

1 Using deformation to recover displacement with Distributed 2 Acoustic Sensing

3 Alister Trabattoni¹, Francesco Biagioli², Claudio Strumia³, Martijn van den Ende¹, Francesco
4 Scotto di Uccio³, Gaetano Festa³, Diane Rivet¹, Anthony Sladen¹, Jean Paul Ampuero¹, Jean-
5 Philippe Métaxian² and Éléonore Stutzmann²

6 ¹ *Université Côte d'Azur, Observatoire de la Côte d'Azur, CNRS, IRD, Géoazur, France* (alister.trabattoni@gmail.com)

7 ² *Institut de Physique du Globe de Paris, Université Paris Cité, Paris, France*

8 ³ *Università di Napoli Federico II, Complesso University Monte S. Angelo, Napoli, Italy*

9 SUMMARY

10 Over a period of less than a decade, Distributed Acoustic Sensing (DAS) has become a well-established
11 technology in seismology. For historical and practical reasons, DAS manufacturers usually provide
12 instruments that natively record strain (rate) as the principal measurement. While at first glance strain
13 recordings seem related to ground motion waveforms (displacement, velocity, acceleration), not all the
14 seismological tools developed over the past century (e.g., magnitude estimation, seismic beamforming, etc.)
15 can be readily applied to strain data. Notably, the directional sensitivity of DAS differs from conventional
16 particle motion sensors, and DAS experiences an increased sensitivity to slow waves, often highly scattered
17 by the subsurface structure and challenging to analyse. To address these issues, several strategies have been
18 already proposed to convert strain rate measurements to particle motion. In this study we focus on
19 strategies based on a quantity we refer to as “deformation”. Deformation is defined as the change in length
20 of the cable and is closely related to displacement, yet both quantities differ from one another: deformation
21 is a relative displacement measurement along a curvilinear path. We show that if the geometry of the DAS
22 deployment is made of sufficiently long rectilinear sections, deformation can be used to recover the
23 displacement without the need of additional instruments. We validate this theoretical result using full-
24 waveform simulations and by comparing, on a real dataset, the seismic velocity recovered from DAS with
25 that recorded by collocated seismometers. The limitations of this approach are discussed, and two
26 applications are shown: enhancing direct P-wave arrivals and simplifying the magnitude estimation of
27 seismic events. While using deformation is in some respects more challenging, converted displacement
28 provides better sensitivity to high velocity phases, and permits the direct application of conventional
29 seismological tools that are less effective when applied to the strain (rate) data.

30 1. INTRODUCTION

31 In recent days, Distributed Acoustic Sensing (DAS) has rapidly gained traction in the seismological
32 community. The technology is used in a wide range of applications across diverse disciplines. The
33 widespread adoption has been greatly accelerated thanks to the availability of ready-to-use telecom dark
34 fibres, and its sensing capabilities in harsh/underwater environments where regular seismometers would
35 have been difficult to deploy and real-time acquisition would be challenging. The DAS technique typically
36 consist in measuring variations of the phase of back-scattered light at each location along an optical fibre
37 to estimate the longitudinal dynamic strain (Hartog, 2017). This provides the equivalent of a uniform, dense
38 array of sensors while deploying only one instrument at one end of the cable. For historical and practical
39 reasons, DAS interrogators natively record strain (or strain rate, its temporal derivative) while traditional
40 seismologic instruments record translational ground motions (displacement, velocity or acceleration).
41 Because strain is a spatial derivative of the displacement, it differs from particle motion in several respects.
42 First, strain measurements have a characteristic directional sensitivity (i.e., a dependence on the direction
43 of propagation and on the particle motion of the recorded wave) with narrower directional sensitivity for
44 P-waves and a clover-like response pattern for S-waves (Martin et al., 2021). Second, strain measurements
45 are more sensitive to slow waves, amplifying highly scattered waves that are difficult to analyse (Trabattoni
46 et al., 2022). And last, finite-gauge length DAS measurements exhibit spectral notches in their instrument
47 response at integer multiples of the apparent phase velocity over gauge length (J. Yang et al., 2022). Most
48 of the tools developed in seismology are adapted to translational ground motion measurements, which may
49 need modification to be used with strain. For instance, magnitude estimation was historically calibrated on
50 the Wood-Anderson seismometer and all magnitude scales require ground displacement inputs. It has also
51 been shown that beamforming can fail on strain data due to the predominance of scattered waves that
52 reduce the wavefield coherence (van den Ende & Ampuero, 2021).

53 For those reasons, several studies have proposed different ways to convert strain to displacement (or other
54 combinations of time derivatives of those two quantities). A first approach is to use the dominant apparent
55 velocity of the observed phases (Daley et al., 2016). The reference velocity is generally estimated to
56 correspond to the moveout of the most energetic phases. This approach has been successfully used for
57 magnitude estimation in both offline and real-time early-warning contexts (Lior et al., 2021, 2023). The
58 main limitation is, however, that only dominant phases are correctly converted. In particular, the relative
59 amplitude between phases with different apparent velocities remains unmodified. This is problematic when
60 the phases of interest have lower amplitudes than the dominant phases. Exact conversion should rebalance
61 the respective amplitude of phases with different apparent velocities. This is particularly useful to enhance
62 body waves that have a much higher apparent velocity relative to shallow scattered waves (van den Ende
63 & Ampuero, 2021).

64 In this study we focus on an alternative way to convert strain to ground motion based on numerical
65 integration along the space dimension. FK rescaling (Daley et al., 2016; Wang et al., 2018; Lindsey et al.,
66 2020; Y. Yang et al., 2022) was a commonly adopted first step in this direction. This method allows one to
67 convert strain to velocity by simultaneously integrating in space and differentiating in time in the FK
68 domain. Here, the amplitudes are weighted by the quantity $-\omega/k$, where ω is the pulsation and k the
69 apparent wavenumber along the cable. Because k can be close to zero all studies that used this approach
70 proposed to dampen small wavenumbers to avoid instabilities and the emergence of spurious low-
71 wavenumber signals. These methods are limited to finite 2D time-space windows, and simultaneously apply
72 a time and a space transformation while sometimes only a space integration would be required (e.g., from
73 strain to displacement or from strain-rate to velocity).

74 Temporal and spatial differentiation/integration can be done separately instead of combining time and
75 space transformation by FK rescaling (note that the FK transformation can be done by applying the Fourier
76 transform twice, in any order, over the time and the space dimensions). We will leave aside the temporal
77 transformation needed to convert strain rate into strain because this problem is the same as converting
78 between displacement, velocity and acceleration, and can be addressed with common methods in the time

79 or spectral domains. The problem of the spatial integration is that the (time-varying) initial value (or the
 80 integration constant) is unknown. Van den Ende & Ampuero (2021) showed that by using co-located
 81 seismometers as reference, the local particle velocity can be estimated along rectilinear segments through
 82 spatial integration of the recorded strain rate. This method is hence limited to setups where co-located
 83 sensors are available. On the other hand, Yang et al. (2022) used a new generation of DAS that can natively
 84 record integrated strain rate, hereafter called “deformation rate”. They observed that integrated
 85 measurements show spurious low-wavenumber signals that can empirically be removed by spatial or FK
 86 filtering methods.

87 Fichtner et al. (2022) laid down a mathematical foundation that explains the origin of the spurious signals
 88 observed in strain-integrated recordings along curvilinear paths. The study focusses on transmission
 89 measurements where the pulse emitted at one end of the cable is recorded by a unique sensor at the other
 90 end of the cable. This type of measurement is not distributed (i.e., sensitive to the strain at each point of
 91 the cable) but integrated (i.e., sensitive to the integrated strain along the cable). The authors show that
 92 strain-integrated measurements are mostly insensitive to the displacement wavefield except at very specific
 93 locations: at the two extremities of the cable (the relative displacement between the two endpoints is
 94 measured) and at each curve or kink of the cable. While this is beneficial for transmission measurements
 95 (Marra et al., 2018), because it allows to retrieve information along the cable (and not only at the endpoints),
 96 the consequences for DAS are not developed.

97 In this study, the theory of deformation measurements along non-rectilinear cables will be presented. Then
 98 concepts will be validated by full-waveform simulations and by comparing DAS recordings with co-located
 99 seismometers deployed at the Stromboli volcano (Italy). Finally, two applications will be presented: body
 100 wave enhancement in a telecom submarine cable laying offshore on the Chilean margin; and direct
 101 magnitude estimation for events recorded by a dedicated cable deployed along the Irpinia fault system
 102 (Southern Italy).

103 2. THEORY

104 The displacement of a body can be decomposed into a rigid-body displacement component and a
 105 deformation component (Fossen, 2016). Rigid-body displacement is the translation and rotation of the
 106 body as a whole. Deformation is the change in shape/size of the body. DAS is sensitive to the latter but
 107 only longitudinally along the cable geometry. In the following, we refer to this curvilinear deformation along
 108 the cable as “deformation”, as proposed by Yang et al. (2022). This quantity is then related to usual DAS
 109 quantities (e.g., strain) and to seismological ground motion quantities (e.g., displacement).

110 2.1. DAS natively measures deformation

111 Let us consider a model fibre-optic cable. Each point of the cable is identified by its curvilinear coordinate
 112 s which is the distance at rest $L_0(s)$ from the DAS interrogator $L_0(s) = s$. If ground displacement occurs
 113 (e.g., due to the passage of a seismic wave) the distance $L(s, t)$ varies. We define the deformation $\delta(s, t)$
 114 as the variation of that distance compared to the undeformed resting distance:

$$\delta(s, t) \equiv L(s, t) - L_0(s) \quad (1)$$

115 For small ground motion, deformation is equal to the curvilinear integration of $\varepsilon(s, t)$ the strain component
 116 along the cable (Fichtner et al., 2022). This latter quantity is equal to the projection along $\mathbf{e}(s)$, the cable
 117 directional vector, of the curvilinear derivative of the displacement $\mathbf{u}(s, t)$:

$$\delta(s, t) = \int_0^s \varepsilon(s', t) ds' = \int_0^s \mathbf{e}(s') \cdot \frac{\partial \mathbf{u}}{\partial s'}(s', t) ds' \quad (2)$$

118 Note that, if not otherwise mentioned, the regular typed symbols are the along-the-cable component of
 119 their bold counterparts, and, that when omitted in a sentence, we refer to those projected quantities.

120 The operating principle of DAS consists in measuring the phase of the backscattered field generated by a
 121 laser pulse to measure scatterers’ displacements. At rest, the phase of the light backscattered from position

122 s presents a random structure $\phi_0(s)$ due to the small and spatially randomised variations of the optical
 123 index of the fibre glass. For a small deformation of the fibre, the optical distances of the heterogeneities
 124 relative to the DAS interrogator change, shifting the phase $\phi(s, t)$ as follows (Hartog, 2017):

$$\phi(s, t) = \frac{4\pi n \xi}{\lambda} \delta(s, t) + \phi_0(s) \quad (3)$$

125 where n is the effective optic index of the fibre, ξ is the photo-elastic coefficient that relates the deformation
 126 of the fibre to changes of its optical index, and λ is the central wavelength in the vacuum of the coherent
 127 laser pulse. Finally, the coefficient $4\pi = 2 \times 2\pi$ considers the fact that light travels back and forth in the
 128 cable and is affected twice by the cable deformation. The unknown $\phi_0(s)$ prevents the recovery of the
 129 static deformation. To get rid of this constant, high pass filtering can be used with a cut-off frequency
 130 related to the frequency content of the signal of interest.

131 More commonly, the temporal derivative of the phase is used to remove the unknown phase reference. It
 132 gives the deformation rate $\dot{\delta}(t, s)$:

$$\dot{\phi}(s, t) = \frac{4\pi n \xi}{\lambda} \dot{\delta}(s, t) \quad (4)$$

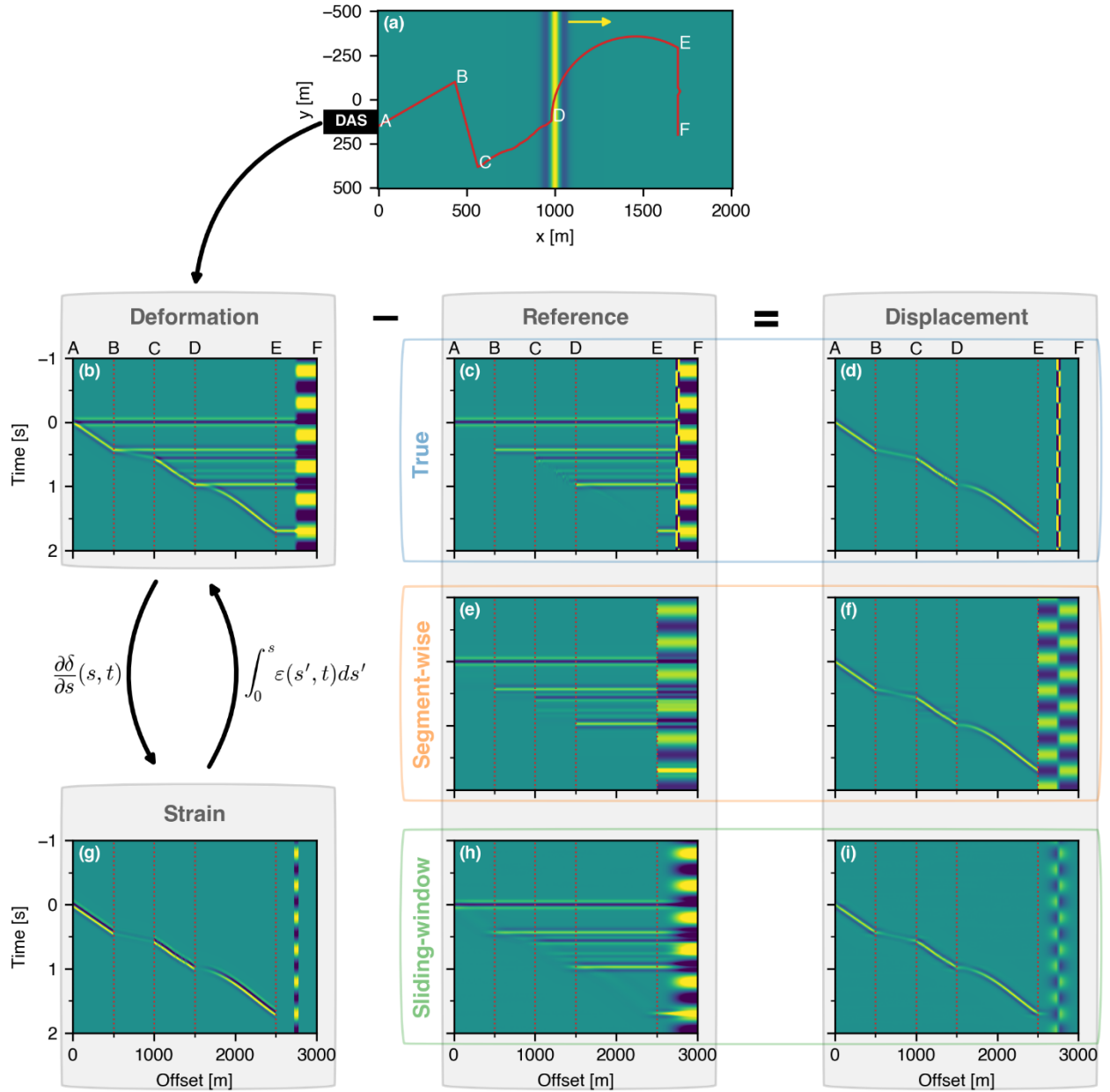
133 Further applying a spatial derivative gives the strain rate $\dot{\epsilon}(s, t)$ which has the advantage of being a local
 134 measurement (see later):

$$\frac{\partial \dot{\phi}}{\partial s}(s, t) = \frac{4\pi n \xi}{\lambda} \dot{\epsilon}(s, t) \quad (5)$$

135 Most modern DAS interrogators use coherent detection techniques and measure phase as a primitive
 136 (Hartog, 2017). They compute derivatives numerically in contrast to direct detection techniques, where
 137 optical interferometric methods are used to make phase comparisons. Spatial differentiation implies a
 138 transfer function that is proportional to the wavenumber. This degrades the low wavenumber sensitivity of
 139 DAS. Numerical differentiation is also known to produce noisier outputs. Smooth derivative schemes are
 140 generally used, (e.g., by averaging the derivative over a spatial window). For most DAS interrogators, the
 141 user can tune the spatial smoothing through the choice of a parameter called gauge length. This latter
 142 quantity damps the high wavenumber signals and can introduce notches to the instrumental response (J.
 143 Yang et al., 2022). The same issues are encountered in the time domain. We will show that deformation,
 144 which is proportional to phase, can be used to directly recover displacement.

145 2.2. Illustration of deformation recordings

146 For didactic purposes, we ran a simple numerical simulation (Fig. 1). A synthetic cable deployment is
 147 exposed to an incoming impulsive plane P-wave made of a 7.5 Hz Ricker wavelet. The medium is
 148 homogenous with P-wave velocity of 1 km/s. The geometry of the cable includes perfect and perturbed
 149 linear sections, kinks, and a curved section (Fig. 1a). It also includes a free-hanging section that is oscillating
 150 (e.g., driven by ocean currents; Mata Flores, Mercerat, et al., 2022; Mata Flores, Sladen, et al., 2022). Strain
 151 (Fig. 1g) appears similar to displacement (Fig. 1d) but it is affected by its comparatively high-pass
 152 wavenumber response. Cable segments where waves arrive with an almost normal incidence (e.g., segment
 153 BC), and consequently a longer apparent wavelength, record lower amplitudes. Deformation was computed
 154 using eq. (7) and curvatures where approximated by an infinitesimal segment-wise rectilinear geometry (see
 155 later). Deformation (Fig. 1b) appears as the superposition of the true displacement field (Fig. 1d) and
 156 horizontal spurious features (Fig. 1c) that prevent the use of deformation as is for seismic waves analysis.
 157 Those features are referred as “non-local” effects.



158
159
160
161
162
163
164
165
166
167
168
169
170
171
172
173
174

Figure 1. Illustrative simulation. (a) An impulsive plane P-wave propagating along the x -axis produces a horizontal displacement wavefield (blue-green-yellow background raster). A fibre-optic cable (red line) records the deformation along a given geometry. DAS interrogators that use coherent detection techniques measure phase which is closely related to (b) deformation. Deformation is the sum of (d) the true displacement and (c) a reference term (also referred to as “non-local effects”) that must be estimated and removed. Non-local effects can be observed as horizontal features. They are space invariant signals starting at a given offset. The origin is either the beginning of the cable (marker A), a kink (markers B, C, D and E), a perturbation of the rectilinear segment (section CD), the curvature of the cable (section DE), or a non-linear effect, here produced by a 50-meter hanging section at the middle of the segment EF. The simulation was tailored so that non-local effects can be visually distinguished but in general they accumulate an overlap, resulting in data that is difficult to interpret. Segment-wise method: The displacement can be closely recovered (f), and the locality of the measurement greatly improved by removing (e) the averaged deformation on each segment (red vertical dotted lines). Few horizontal artifacts can be seen (e.g., on segment CD). Sliding-window method: An alternative solution is to remove (h) a sliding average (here 500 m is used with a Hann tapering) to get (i). Artifacts (or border effects) can be observed at some kinks. Spatial differentiation of the deformation gives (g) strain which is a local measurement.

175 2.3. Non-locality of the deformation

176 A non-local measurement implies that a measurement made at a given location depends on the value of the
 177 field of interest at other locations. Deformation is non-local for two reasons: the lack of a proper reference
 178 (referred to as “reference error”) and changes in cable direction (referred to as “geometric effects”).

179 Let us consider the simple case of a rectilinear geometry (Fig. 2a and segment AB in Fig. 1). Integrating eq.
 180 (2) with constant direction $\mathbf{e}(s)$ shows that, in this configuration, the deformation is the difference of the
 181 displacement $\mathbf{u}(s, t)$ between the two integration limits:

$$\delta(s, t) = \mathbf{u}(s, t) - \mathbf{u}(0, t) \quad (6)$$

182 Deformation gives the displacement relative to a reference which is the displacement of the beginning of
 183 the cable. If $\mathbf{u}(0, t)$ is zero, the deformation is equal to the displacement (Fig. 2c). Otherwise, the motion
 184 of the reference point produces a spatially-constant (but time-varying) additive term on all measurement
 185 points (Fig. 2b). This reference error appears as a horizontal space-invariant signal that affects the whole
 186 cable (from marker A to F in Fig. 1b).

187 Along a rectilinear cable, the displacement of one point of the fibre generates an equal amount of positive
 188 strain on one side and negative strain on the other side (Fig 2c). When integrating through, the two
 189 contributions cancel out making subsequent measurement points insensitive to the displacement of that
 190 point. This is no longer the case when the cable is not rectilinear: the displacement of a point of the cable
 191 located at a kink produces an unbalanced amount of strain (Fig. 2d).

192 For a segment-wise rectilinear geometry, the overall deformation is the sum of the deformation of each
 193 rectilinear segment up to the point of interest s . Splitting the integral in eq. (2) per segment and applying
 194 eq. (6) per segment, this can be expressed as:

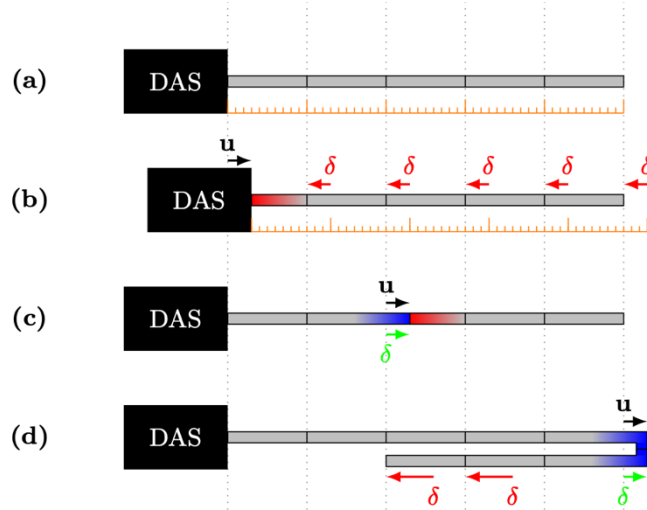
$$\delta(s, t) = \mathbf{u}(s, t) - \sum_{k=1}^n [\mathbf{u}(s_k^+, t) - \mathbf{u}(s_k^-, t)] - \mathbf{u}(0, t) \quad (7)$$

195 where s_k are the locations of the kinks and n is the number of kinks preceding the location s . At each kink
 196 a new additive constant term appears and impacts all subsequent measurement points. Those terms are
 197 equal to the difference between the displacement along the direction before (subscript $-$) and after
 198 (subscript $+$) the kinks. It changes the reference against which the displacement is measured. Those
 199 geometrical effects appear as horizontal space invariant features that start at each kink location (at markers
 200 B, C, D and E, and along the non-rectilinear CD segment in Fig. 1b).

201 For the general case of a curved cable, it can be shown that integrating eq. (2) by parts (Fichtner et al., 2022)
 202 gives:

$$\delta(s, t) = \mathbf{u}(s, t) - \int_0^s \frac{\partial \mathbf{e}}{\partial s}(s) \mathbf{u}(s, t) ds - \mathbf{u}(0, t) \quad (8)$$

203 The term $\partial \mathbf{e} / \partial s(s)$ represents the sharpness in change of direction. This implies that the radius of
 204 curvature plays a central role in the amplitude of this effect (the geometric effect related to the smoothly
 205 curved section DE is for example not very pronounced in Fig. 1c).



206

207

208

209

210

211

212

213

214

215

216

217

218

219

220

221

Figure 2. Non-locality of the deformation. (a) A rectilinear fibre-optic cable (grey line) that is at rest. Reference markers (black ticks) are placed at regular distances of the DAS (orange ruler). Let observe three snapshots of the passage of a zero-average localised impulsive wavelet propagating through the cable from left to right. (b) The ground displacement starts to reach the beginning of the cable (blue is elongation, red contraction). The displacement of the instrument produces a contraction of the beginning of the cable that reduces the distance to all subsequent points of the cable. A constant deformation $\delta(s, t) = -u(0, t)$ is added to the entire cable. (c) The deformation is then confined inside the linear section. Because the contraction on one side is equal to the elongation at the other side, the integrated strain cancels out and subsequent point remain unaffected. Since in that case the reference point (the DAS interrogator) also does not move, the measurement is local: $\delta(s, t) = u(s, t)$. (d) Eventually, the impulse reaches the end of the rectilinear section. If the cable continues with a kink (here with a 180° angle), the elongation is no longer compensated by an equal contraction (that here lies outside of the cable). In the case presented here, it is the opposite: the backward part of the kink is elongated with the same amount. The arc length to reach points located after the kink is augmented by twice the displacement of the kink $\delta(s, t) = 2u(s, t)$. This is a typical example of geometric effect showing that integration cannot be applied as is across a kink.

222

223

224

225

Non-local effects disappear once spatial differentiation is applied (eq. 5) making strain (rate) a local measurement (Fig. 1g) since every measurement is compared to its neighbours. Next, we show that it is possible to reduce the non-locality of deformation and approximate the displacement by applying suitable processing.

226

2.4. Recovering displacement from deformation

227

228

229

230

231

232

233

234

235

236

We have seen that deformation is a measure of displacement relative to a reference that is unknown and related to the displacement of the start and the kinks (or curved portions) of the cable. This leads to spurious signals that appear as additive terms which are space-invariant over each rectilinear segment (Fig. 1b). By contrast, seismic signals exhibit a finite wavelength of variation (Fig. 1d) that – if averaged over a sufficient length scale – has zero spatial mean. To approximate the non-local effects (Fig. 1c), one solution is then to compute the spatial mean over each rectilinear segment (Fig. 1e). This estimate of the reference can then be removed from the deformation to estimate the displacement (Fig. 1f). We will refer to this first approach as the “segment-wise” method. Applying this process to eq. (7) show that the obtained estimate of the displacement $\hat{u}(s, t)$ is the displacement $u(s, t)$ minus its spatial average $\bar{u}_n(t)$ over the n -th segment related to the location s :

$$\hat{u}(s, t) = \delta(s, t) - \bar{\delta}_n(t) = u(s, t) - \bar{u}_n(t) \quad (9)$$

237

238

239

240

We set as reference the spatial average, essentially replacing an arbitrary reference with one that approximates to zero if the wavelength of the signals of interest is much shorter than the length of the rectilinear section of the cable (see later). The mean can be computed using a weighting (or tapering) window $w_n(s)$ that integrates to one and has zero values outside the n -th segment (see later):

$$\bar{\delta}_n(t) = \int w_n(s')\delta(s', t)ds' \quad (10)$$

241 Unfortunately, deploying linear sections of cable is often impractical and, in many cases, the user has only
 242 limited knowledge on the cable geometry (e.g., for submarine cables). In those cases, a more flexible
 243 approach is to choose a characteristic length over which we expect the cable to be approximately linear.
 244 Then for each cable location, the reference is estimated by removing a local sliding average (Fig. 1g-h):

$$\hat{u}(s, t) = \delta(s, t) - (w * \delta)(s, t) = u(s, t) - (w * u)(s, t) \quad (11)$$

245 where $*$ denotes the convolution along space and w is a chosen weighting window. This second approach
 246 will be referred to as the “sliding-window” method. To get the values at the ends of the cable, padding is
 247 necessary with this approach. Several padding strategies can be used: filling with zeros, with the edge value,
 248 or by reflecting values (using mirrored values on the edge). The choice of the padding mode only affects
 249 the beginning and the end of the cable and do not appear to have significant consequences. The reflecting
 250 mode seemed to generally work better and was used in this study (see later, supplementary material, Fig.
 251 S1).

252 The two proposed methods reduce the non-locality of the deformation measurements. The segment-wise
 253 scheme limits the non-locality to the size of each segment: the value of the displacement at one location of
 254 the cable only affects the values measured within its segment. The sliding-window scheme limits the non-
 255 locality to the width of the chosen sliding window. This can be important for example in case of highly
 256 corrupted channels (e.g., the hanging cable in Fig. 1f, i) that will only impact a finite width of the cable. On
 257 the other hand, the use of Infinite Impulse Response (IIR) filters to perform average removal or (high-pass
 258 filtering) theoretically spreads those errors indefinitely.

259 2.5. DAS sensitivity to displacement

260 The displacement that is recovered in the manner described above only approximates the true displacement.
 261 In particular, the mean removal affects the low wavenumber response of the recovered displacement. We
 262 will focus on the sliding-window method, but similar results can be showed for the segment-wise method.
 263 Using the convolution theorem in eq. (11), the sensitivity can be expressed as:

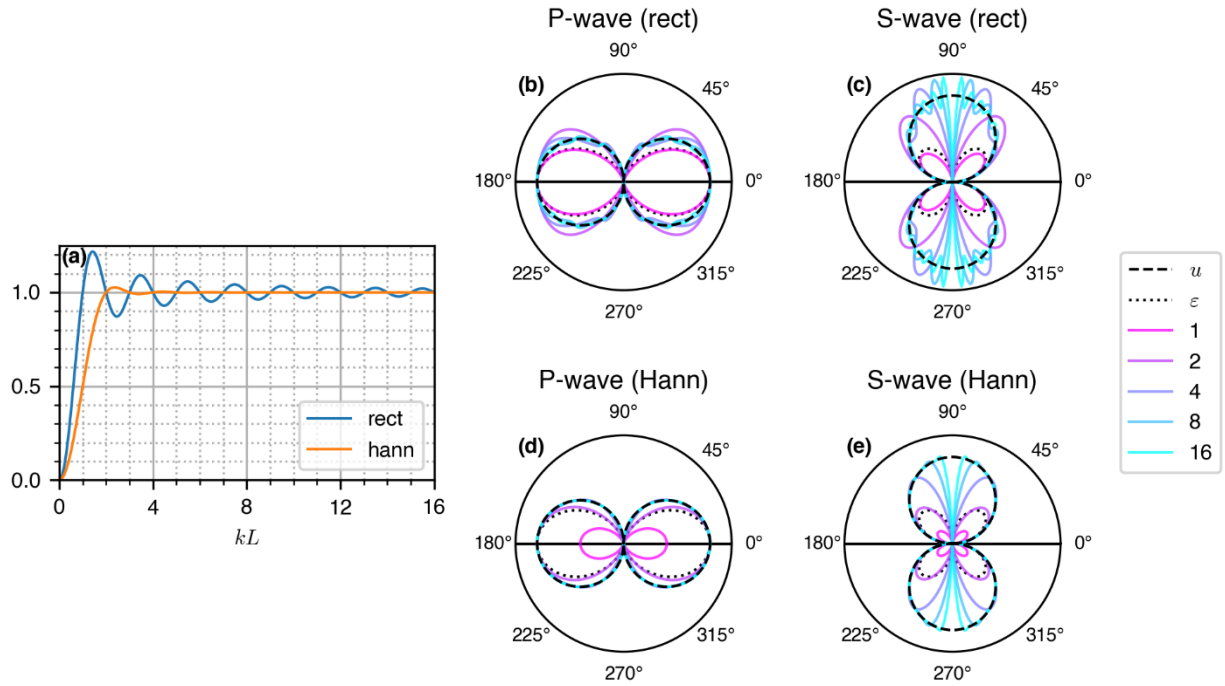
$$\hat{U}(k, t) = (1 - W(k))U(k, t) \quad (12)$$

264 where uppercase letters are the spatially Fourier transformed versions of their lowercase counterparts, and
 265 k is the apparent wavenumber along the cable.

266 Depending on the choice of $w(s)$ the response varies, but some common features are always retrieved.
 267 Owing to the relative measurement principle of DAS, rigid-body displacements cannot be recovered.
 268 Consequently, displacements of wavelengths that exceed the length of rectilinear sections (approaching the
 269 limit of rigid-body translation), cannot be retrieved. On the other hand, wavelengths that are much shorter
 270 than the typical rectilinear length tend to average out along the cable length and relative motion of the
 271 different parts of the cable can be correctly measured. This mandates the use of long linear segments for
 272 studies focused on measuring long apparent wavelengths.

273 The choice of the optimal weighting function w depends on the nature of the signal and the objective of
 274 the analysis. Using a rectangular window implies a sinc weighting function in the wavenumber domain
 275 which ensures minimal low wavenumber sensitivity but generates prominent side lobes (Fig. 3a). The use
 276 of a smoother weighting function like the Hann window deteriorates the smallest recoverable wavenumbers
 277 but significantly reduces the presence of side-lobes, ensuring a much flatter response (Fig. 3a).

278 Because the apparent wavenumber depends on the angle of incidence at which the incoming wave strikes
 279 the cable, eq. (12) implies a directional sensitivity (Fig. 3 b-e). Waves orthogonal to the cable have infinite
 280 wavelength and cannot be recovered, regardless of their frequency content. This is already the case for P-
 281 waves where a single component displacement measurement results in zero sensitivity in the orthogonal
 282 direction. For S-waves this produces the presence of a notch whose width depends on the relative size of
 283 the wavelength of interest with the length of the rectilinear section, and on the chosen tapering (Fig. 3c, e).



284
 285 **Figure 3.** Sensitivity characteristics of deformation-recovered displacement. (a) The sensitivity is a function
 286 of the product between the apparent wavenumber and the length of the rectilinear section (kL); and the
 287 shape of the window (here rectangular and Hann windows are shown). Rigid-body displacement cannot be
 288 recovered (zero wavenumbers) by DAS. The shape of the window affects the recovered displacement, and
 289 its selection requires a compromise between a flat response (no side-lobes) and a strict low cut-off
 290 wavelength. Because the apparent wavenumber is a function of the angle of incidence, a directional
 291 sensitivity pattern is implied. (b), (c), (d) and (e): Directivity patterns for plane P- and S-waves for the
 292 rectangular and the Hann windows for different kL values (from 1, magenta lines, to 16, cyan lines – see
 293 legend on the right). The horizontal black line indicates the cable direction. For P-waves, the sensitivity
 294 converges toward the response of the desired displacement (black dashed line) as kL increases. For S-
 295 waves, waves with orthogonal incidence to the cable have infinite apparent wavelength making their
 296 recovery physically impossible. Consequently, the sensitivity of S-waves exhibits a notch at orthogonal
 297 directions of the cable that get thinner as kL increases. Note that the rectangular window converges twice
 298 faster and has a twice smaller notch than the Hann window but generates significantly more ripples.

299 3. VALIDATION

300 In this section, we validate the proposed displacement (or velocity) recovery method using full waveform
 301 simulations, and through comparison with data acquired on the Stromboli volcano by both DAS and co-
 302 located seismometers.

303 3.1. Full-waveform simulation

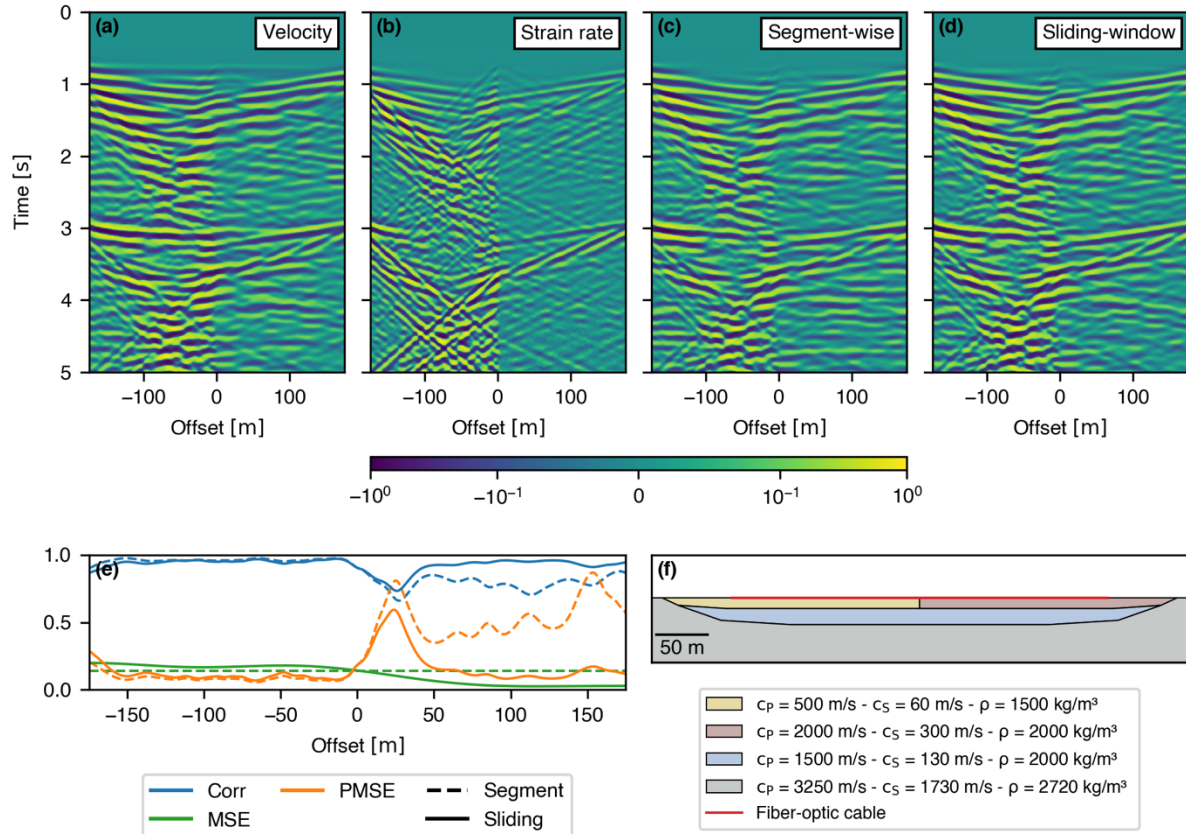
304 To evaluate the capacity of DAS to recover velocity instead of the natively provided strain rate, a full-
 305 waveform simulation was used to model complex and realistic wavefields. We modelled waves propagating
 306 through a shallow sedimentary basin that represents a common situation for DAS deployments both on-
 307 land and off-shore. Sedimentary basins produce complex wavefields because ballistic waves are distorted,
 308 amplified, trapped, and cause interference among each other.

309 We used the geometry proposed in Trabattoni et al. (2022) that corresponds to the case of a dedicated
 310 deployment located in the Irpinia Near-Fault Observatory (INFO, Southern Italy). It consists of a two-
 311 layer basin of 25 m depth resting on the bedrock (Fig. 4e). To test the influence of shallow heterogeneities
 312 beneath the cable, the original model was modified by laterally extending the basin and by including an
 313 abrupt lateral change in phase velocity in the upper layer.

314 We simulated the wave propagation in the basin using SPECFEM2D (Tromp et al., 2008). The source
315 consisted of two plane waves (P and S) with identical angle of incidence (40°) and source time function (5
316 Hz Ricker) but delayed by 2 s and with different polarities. A 350 m long virtual cable was located at the
317 centre of the basin. The horizontal component of the velocity was evaluated at the surface every 0.5 m with
318 a sampling rate of 200 Hz (Fig. 4a) and used to estimate the deformation (see Appendix B), the DAS
319 measured strain rate (Fig. 4b), and the DAS recovered velocity (Fig. 4c and d). The latter was obtained
320 using both the segment-wise (eq. 9) and the sliding-window (eq. 11) approaches with the same Hann
321 window whose width was set to the entire length of the cable. Reflection-mode padding was performed to
322 obtain estimates at the cable's extremities (see other padding modes in the supplementary material, Fig. S1).

323 The velocity wavefield is dominated by high apparent velocity direct and multiple P and S waves (Fig. 4a).
324 The strain rate wavefield enhances low velocity surface and refracted S waves propagating in the basin and
325 increases the amplitude contrast between both sides of the basin (Fig. 4b). Both recovered velocities visually
326 match well with the true velocity. Only the phases with the highest apparent velocities are not perfectly
327 retrieved. The first arrival, which has a particularly high apparent velocity and low energy, is partially
328 recovered especially with the segment-wise approach.

329 To quantify the error, several metrics were applied at each channel (Fig 4d): the Mean Square Error (MSE),
330 Percentage MSE (PMSE: the MSE divided by the mean square of the reference) and the correlation
331 coefficient (CC). The MSE – which is minimized by mean removal – is constant for the segment-wise
332 approach because the same reference error occurs at each location (i.e., a single reference value is estimated
333 for the entire cable). For the sliding-window approach its value varies with slightly worse results on the
334 high amplitude/low velocity first half of the basin but with much smaller errors in the low amplitude/high
335 velocity section. This result highlights that the segment-wise estimation is driven by the high amplitude
336 areas and that the sliding-window approach better adapts to subsurface wave speed variations. Because of
337 this amplitude contrast, relative metrics (PMSE and CC) better capture the recovery performance. Both the
338 PMSE and CC highlight the difference between the two approaches but also reveal increased errors at the
339 extremities of the cable and at the location of the subsurface discontinuity. The median CC and PMSE are
340 respectively 0.90 and 20% for the segment-wise scheme and, 0.95 and 11% for the sliding-window scheme.
341 Note that the relative effectiveness of one scheme over the other is scenario-dependent.



342
 343 **Figure 4.** Full-waveform simulation for a shallow sedimentary basin configuration. (a) Simulated particle
 344 velocity along the cable. (b) Strain rate along the cable. (c) and (d) Recovered particle velocity along the
 345 cable with the segment-wise and the sliding-window methods. While strain rate is almost insensitive to long
 346 wavelengths, the phases with high apparent speed are remarkably well reconstructed after the conversion
 347 process. Yet, near horizontal arrivals are hardly retrieved since they are associated with high apparent
 348 wavelengths, comparable or longer than the fibre extension. (e) Error metrics along the fibre. The error is
 349 larger in the higher speed area because waves have inherently longer wavelengths and lower amplitudes (f)
 350 The geometry of the basin, composed of two soft layers superimposed on the bedrock. The speed of the
 351 most superficial layer is increased over one half of the basin, to simulate an abrupt wave speed change
 352 beneath the cable.

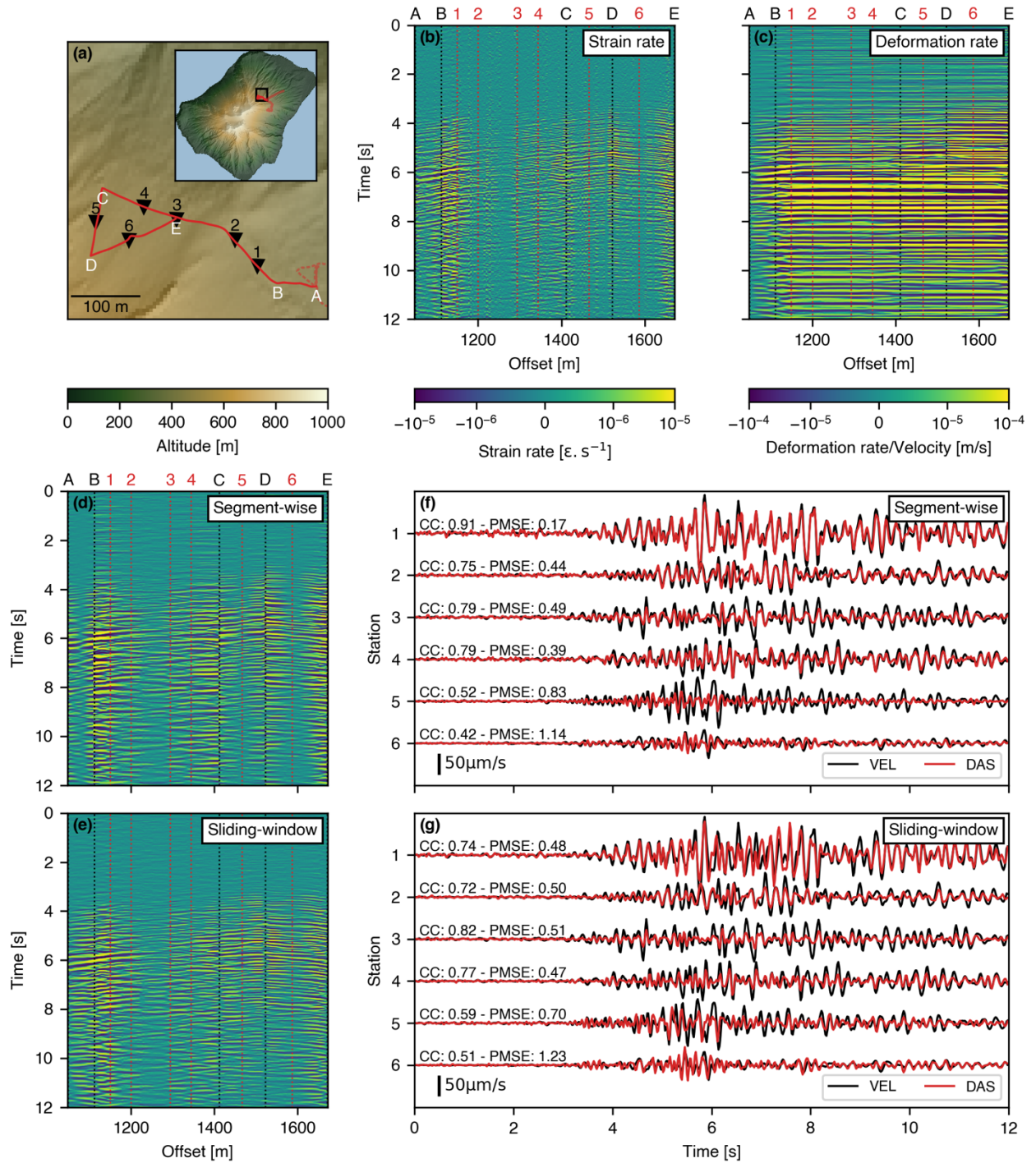
353 3.2. Comparison with co-located seismometers

354 To further validate and better illustrate our theoretical developments, we applied our methodology to an
 355 experiment with a dedicated fibre-optic cable deployed on the Stromboli volcano. In this experiment, DAS-
 356 recovered velocities could be compared with traces recorded by co-located seismometers. A 3 km fibre-
 357 optic cable was deployed on the northeast flank of Stromboli to monitor the volcano activity (Biagioli et
 358 al., submitted). The data presented here was acquired in September 2021 by a Febus A1-R DAS interrogator
 359 parametrised with a gauge length of 4.8 m, a differentiation time of 10 ms, a repetition rate of 10 kHz
 360 decimated to a sampling rate of 200 Hz and a channel spacing of 2.4 m. This study focuses on a 600 m
 361 portion of the cable composed of relatively rectilinear segments where six co-located three-component
 362 nodes (SmartSolo IGU-16HR with 5 Hz corner frequency and sampling at 250 Hz) were deployed at the
 363 middle of the segments (Fig 5a). The recordings of an explosive event of mild intensity that occurred at
 364 20:47:03 UTC on 26 September 2021 were studied.

365 To compare DAS with nodal seismometer data, the recordings were decimated to a common sampling rate
 366 (50 Hz) and filtered between 2.5 and 15 Hz (limited by the noise floor of the DAS instrument). The
 367 instrumental response of the seismometers was removed and the 3D particle velocity was projected along
 368 the direction of the cable. The strain rate recorded by DAS (Fig. 5b) was multiplied by a calibration factor

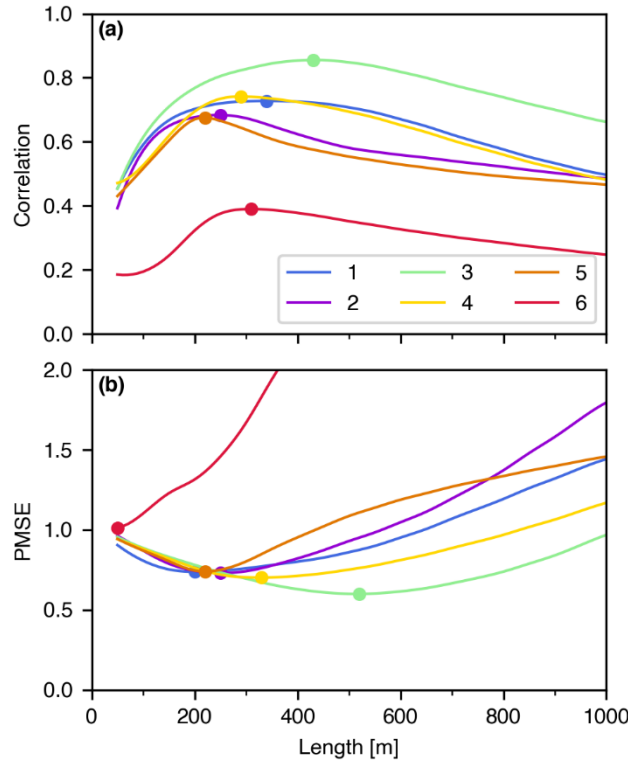
369 of 2.5 (see Biagioli et al., submitted for more details). Strain rate was integrated spatially to get the
370 deformation rate (Fig. 5c). The latter is severely affected by spurious signals which accumulate at each
371 change in cable direction. Velocity was then recovered by applying both the segment-wise (Fig. 5d) and the
372 sliding-window (Fig. 5e) approaches. For the segment-wise approach, the segment limits were manually
373 identified (noted A-E). Because it reduced the recovery performance metrics (see later), one gradual change
374 in the orientation of the cable (between B and C) was not considered as a kink, and the BC segment was
375 treated as a single straight section. This suggests that a compromise between the segment length and its
376 rectilinearity must be found. For the sliding-window scheme, the choice of the optimal Hann window
377 length (250 m) was estimated by computing, for varying window lengths, the PMSE and the correlation
378 coefficient (CC) between the velocity recovered from DAS and that recorded by the seismometers for each
379 seismometer (Fig. 6). The window length must ideally be longer than the apparent wavelength of the
380 recorded waves and smaller than the characteristic rectilinear length of the cable geometry. Results show
381 that indeed the optimal window length is constrained to the longest rectilinear segment length that can be
382 centred on the channel of interest. Finally, the DAS channels closest to each seismometer (indicated as #1-
383 6) were extracted for a direct comparison with the co-located seismometers (Fig 5e and g).

384 Using either recovery approach, the recovered DAS velocity waveforms exhibit an acceptable agreement,
385 both in phase and in amplitude, with the seismometer recordings. The worst results are found at station
386 #6. This receiver was located on a segment featuring a strong bend in the cable made to avoid an outcrop
387 of more competent rocks. We therefore attribute the poor performance at this station to strong geometrical
388 effects. Likewise, station #5 was located along the shortest segment (DC) and compares poorly to the
389 recovered DAS velocities. This is likely owing to the short length of the segment and the presence of a
390 connection box that introduced a small T-shape like geometric perturbation. For the other stations, the
391 correlation coefficients (CC) typically range between 0.7 and 0.8, reaching 0.9 at the station #1, with the
392 segment-wise scheme. Both the sliding-window and segment-wise approaches provides similar results in
393 terms of PMSE and CC. Looking at the DAS data in space-time plots, the segment-wise approach visibly
394 exhibits horizontal artifacts (e.g., before the event, close to the borders of the BC segment in Fig. 5d) and
395 wavefield discontinuities at the segment limits (e.g., for the strongest arrival at marker B in Fig. 5d), that
396 arise from the fact that the average is removed simultaneously on all channels and that each segment is
397 treated independently. The performance of the two approaches depends on several factors, such as the
398 geometry of the deployment, the lithology, the coupling and the selection of one approach depends on the
399 wavefield of interest and the aim of the analysis.



400
 401 **Figure 5.** Comparison between velocities recovered from DAS and co-located-seismometers. (a)
 402 Deployment of the fibre-optic cable across the north-east flank of Stromboli volcano, with a detail of the
 403 fibre section considered in this study (solid red line). Six nodes were deployed (#1-6) at the midpoints of
 404 the straight segments (black inverted triangles). Letters from A (i.e., the beginning of the cable section) to
 405 E (its end) mark the sharp changes in orientation. (b) Strain rate recorded along the considered cable
 406 segment. Dashed black lines individuate the changes in cable direction marked in (a). Red dotted lines
 407 represent the offsets of the DAS channel closest to each seismometer. (c) Deformation rate without any
 408 processing. (d) Velocity recovered with the segment-wise approach using the A-E markers as segment
 409 limits. (e) Velocity recovered with the sliding-window approach with a 250 m Hann window. (f-g)
 410 Comparison between the velocity waveforms from the seismometers (in black) and recovered from DAS

411 (in red), described by means of correlation coefficient (CC) and the PMSE, for the segment-wise and
 412 sliding-window approaches respectively.



413 **Figure 6.** Search of the optimal window length L^* . DAS-recovered velocity computed with different
 414 window lengths using the sliding window approach was compared to the ground velocity recorded at the
 415 six co-located seismometers (#1-6). Two comparison metrics were used: (a) PMSE; and (b) Correlation
 416 Coefficients (CC). Circles mark the optimal values for each channel. We found a correlation between the
 417 segment lengths and the value of L^* . Channel #5 is located on the smaller segment (DE) and have the
 418 smaller L^* . Its L^* is twice its segment length because the effective length of the Hann window is half its
 419 size. Channel #3 is in the middle of the longest section (BC) and present the longer L^* of 450 m. Channels
 420 #1 and #4 – being closer to their segment end – have smaller L^* . Channel #2 is almost on a smooth turn
 421 and also have intermediate L^* . The distance to the closest edge seems to be the main factor dictating L^* .
 422

423 4. APPLICATIONS

424 Two applications of the use the deformation will be presented. The first one shows that deformation allows
 425 to enhance direct body P-waves that are otherwise difficult to observe in strain rate data. The second one
 426 shows how magnitude estimation is facilitated using deformation because it permits the use of traditional
 427 seismologic methods.

428 4.1. Direct P-waves enhancement

429 In and around sedimentary basins, distributed strain rate measurements are known to be sensitive to site-
 430 effects and mainly record highly scattered/refracted phases (Trabattoni et al., 2022). We will show here that
 431 deformation measurements improve the sensitivity to waves with higher apparent speeds and allow one to
 432 observe phases that are otherwise indistinguishable.

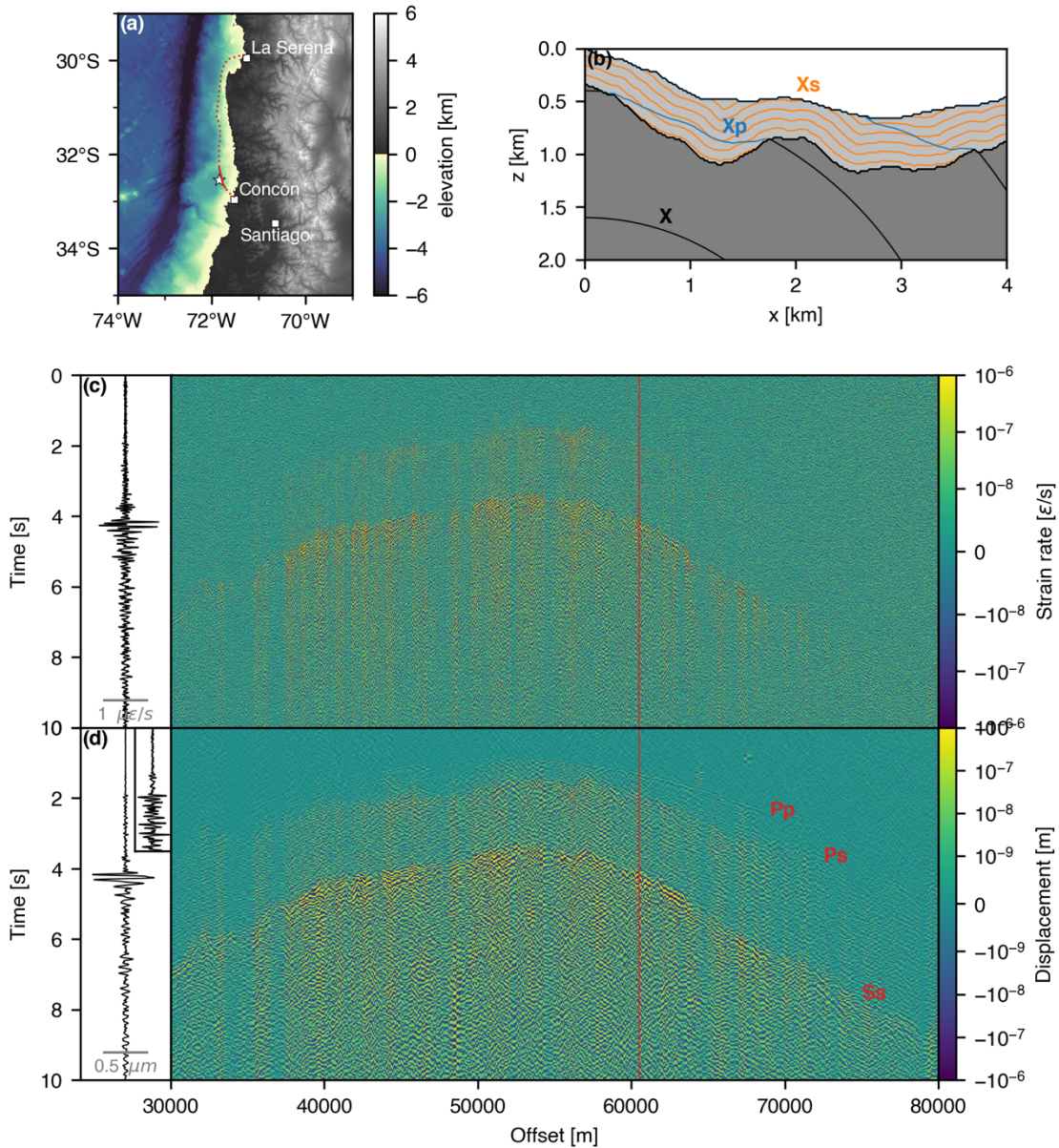
433 Sedimentary basins can be found both on land and off-shore. We will focus on a small regional earthquake
 434 recorded during a deployment that took place offshore Chile (Fig. 7a). A DAS interrogator (OptoDAS –
 435 Alcatel Submarine Networks) was connected in Concón during the month of November 2021 to the
 436 submarine fibre optic telecom cable (operated by GTD group) that links Concón to La Serena. A gauge

437 length of 8.16 m was used with a repetition rate of 625 Hz decimated to a sampling rate of 125 Hz and a
 438 spatial sampling of 4.08 m.

439 Both P and S phases arriving to the bottom of the basin are either converted or transmitted. Because of the
 440 very slow velocity of S-waves in sediments and hence the high P to S velocity ratio, S-waves get much more
 441 amplified and distorted than P-waves (Fig. 7b). This results in the dominance of slow refracted/scattered
 442 waves. Because of the high sensitivity to slow waves of strain rate measurements, this is further exacerbated
 443 (Fig 7c). When converting data to displacement (using the sliding-window scheme with a 1 km Hann
 444 window) the increased sensitivity to faster waves allows the observation of faint waves that travel as direct
 445 P-waves in the sediments (Fig. 7d). Also, the overall signal-to-noise ratio improves (see supplementary
 446 material, Fig. S2). The analysis of the direct, coherent P arrival potentially enables the use of array processing
 447 techniques such as beamforming (van den Ende & Ampuero, 2021).

448 Because the P transmitted P arrival (Pp) is less distorted, it provides a much better estimate of the P-wave
 449 arrival time. Studying the arrival time difference between Pp and the P converted S (Ps) phases should
 450 provide information on the sedimentary structure. Finally, the use of the Pp phase should enable more
 451 accurate location procedures.

452



453

454 **Figure 7.** Application of the use of the deformation to recover displacement. (a) Geographic context of
455 the deployment. A submarine telecom cable (dashed red line) was instrumented from Concón. Here only
456 the data coming from the section between 30 and 80 km away from the instrument was used (red solid line)
457 to record a small regional event that occurred very close to the cable (white star: probable location;
458 magnitude was not estimated). (b) Illustration of the strong deformation and amplification of any incoming
459 phase X into a converted/transmitted S-wave (noted Xs) while the P-wave (noted Xp) get less distorted.
460 (c) Strain rate. We mainly see the increased high frequency and wavenumber instrumental noise along with
461 slow, strongly scattered waves. On the left inset, the trace of the channel located at offset 61 km (red solid
462 line) is displayed. We mainly see the Ss arrival. (d) Displacement recovered using a 1 km sliding Hann
463 window. The noise is reduced, and slow apparent velocity waves are enhanced. This allows for the direct
464 P-wave phase (noted Pp) to emerge from the noise. On the left inset, the trace of the channel located at 61
465 km (red solid line) is displayed. We see three arrivals. A zoom on the first 3.5 s is showed to highlight the
466 Pp arrival. Both recordings (strain rate and displacement) have been filtered above 5 Hz to remove the
467 micro seismic noise contribution.

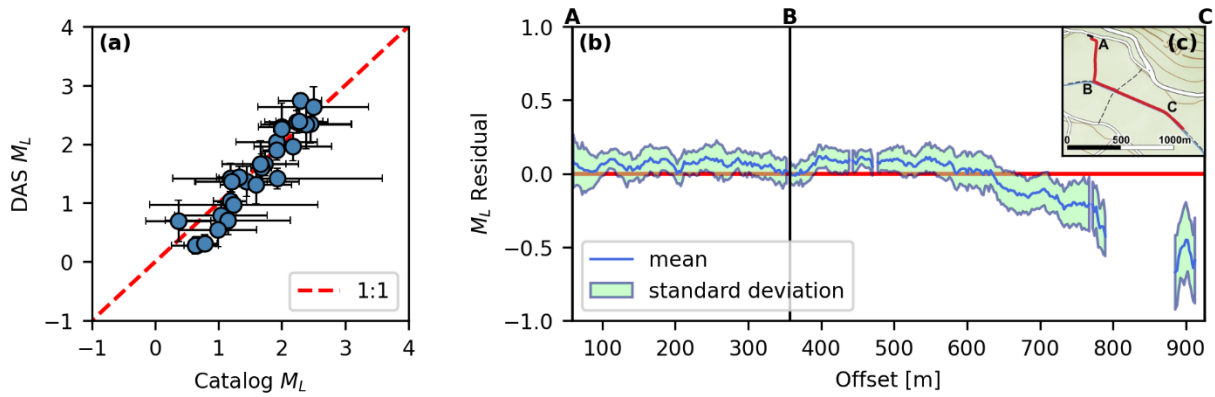
468 4.2. Magnitude estimation

469 Most methods that estimate the magnitude of an earthquake rely on the amplitude of particle motion
470 recordings. We propose to use DAS recovered displacement to directly estimate the local magnitude (M_L)
471 of small earthquakes recorded during the experiment presented in Trabattoni et al. (2022). A 1.1 km long,
472 L-shaped fibre (Fig. 8c) was installed in the active tectonic area of the Southern Apennines (Italy), in the
473 region affected by the 1980 Irpinia M6.9 earthquake. It was integrated within the Irpinia Near Fault
474 Observatory (INFO) which is composed of 31 permanent seismological stations. The experiment
475 continuously recorded earthquakes and ambient noise for almost five months from September 2021 to
476 January 2022.

477 Seismic events were extracted from the DAS records using origin times from the INFO catalogue. Strain
478 rate recordings were filtered between 1-30 Hz, and then converted to deformation rate through spatial
479 integration (eq. 2). The sliding-window scheme was used with a window length of 250 m to recover the
480 velocity. Assuming a flat frequency response for the fibre, velocity traces were transformed into Wood-
481 Anderson displacements by time integration and by applying the specific Wood-Anderson instrumental
482 response. We independently estimated the local magnitude for all the channels along the fibre using the
483 scale tailored for the Irpinia area $M_L = \log_{10} A + 1.79 \log_{10} R - 0.58$ (Bobbio et al., 2009). Here A is the
484 maximum peak amplitude of the Wood-Anderson displacement, and R is the hypocentre distance (in km).

485 We selected DAS usable channels according to their Signal to Noise Ratio (SNR), evaluated as the ratio
486 between the maximum amplitude A and the Root Mean Square (RMS) of the 20 s period preceding the
487 origin time of the event. Only channels meeting a SNR criterion of 5 were considered. Events where less
488 than 30 channels did meet that criterion were discarded, reducing the number of usable earthquakes from
489 about one hundred to 29 events. The final magnitude was estimated as the median value of the M_L
490 distribution at all the usable channels $\widetilde{M}_L = \text{median}(M_L(s))$. To quantify the uncertainties, the SMAD
491 (Standard Median Absolute Deviation) over the different available channels were computed as $\text{SMAD}(s) =$
492 $1.4826 \times \text{median}(|M_L - \widetilde{M}_L|)$. For comparison, the same process was applied to the traces recorded by
493 the INFO network.

494 Magnitude estimates provided by the DAS match those computed from the INFO network (Fig. 8a)
495 showing that using DAS recovered velocity enables simple and accurate M_L estimation. This workflow
496 avoids the need of inverting any effective velocity, provides correct magnitude estimation and is
497 computationally efficient.



498 **Figure 8.** M_L estimation from DAS-recovered velocity. (a) Comparison between DAS and INFO estimates, with associated uncertainties (SMAD). The results are compatible with a 1:1 curve. DAS estimations have lower uncertainty probably because DAS samples a small spatial extent with more correlated hence potentially biased measurements. (b) Mean residual at each channel along the fibre. The curve is represented in between the standard deviation of the residuals, and only channels where M_L has been estimated for a minimum of 10 events have been used for this analysis. The SNR decreases at the last channels of the fibre, likely due to the influence of the basin structure. The vertical lines represent the separation between the main segments of the Irpinia DAS array, showed in (c). DAS estimations are quite stable along the majority of the cable despite a change of the nature of the subsurface between section AB (cultivation field) and BC (dirt road).

509 Looking at the variability of the estimated magnitude along the cable for different events the estimated magnitudes are quite stable for a major part of the cable (Fig. 8b): The estimates of the last segment decrease progressively, maybe due to local site effects and attenuation, for which the calibrated magnitude scale may be inappropriate. This trend could be removed to improve the magnitude estimation.

513 5. CONCLUSION

514 While the standard output provided by most DAS interrogators is provided in strain (rate), here we propose to use the deformation (rate) which is the spatial integral of the strain (rate) along the cable. The deformation is closely related to the displacement but presents crucial differences. Deformation is a measure of the change in length of the cable and provides a displacement measurement relative to a reference. If the reference is non-zero, the inferred deformation no longer equals the true particle motion at a given location on a DAS cable. As a result, spatially-constant offsets appear in the estimated displacement data, and accumulate along the cable. To recover the true displacement from the deformation, without direct access to a reference (as e.g., provided by co-located seismometers), two methods are proposed. When the cable geometry is known, estimating and removing the spatial mean of the signal for each rectilinear segment effectively eliminates the reference; we refer to this method as the segment-wise method; If the cable geometry is poorly known or cannot be readily approximated by linear sections, a sliding average (sliding-window method) continuously estimates and removes the reference from the deformation data. The performance of each method is comparable but situationally-dependent. Nevertheless, owing to its flexibility and the reduced presence of artifacts we recommend the sliding-window scheme as standard conversion procedure.

529 Displacements recovered from deformation provide an instrumental sensitivity that, compared to strain, presents several benefits: (i) it is compatible with standard seismological tools, (ii) it is more sensitive to long apparent wavelength signals and has a broader directivity pattern, (iii) it is proportional to the phase of the backscattered light which is the primitive measurement provided by most modern DAS interrogators that uses coherent detection techniques hence. On the other hand, deformation-based methods are limited by the rectilinearity of the deployed fibre optic cable. The maximum recoverable wavelength by a rectilinear

535 section is directly linked to its length. This should encourage the use of geometries with long rectilinear
536 segments.

537 The benefits of deformation-recovered displacement are highlighted for two use cases. It allows direct non-
538 scattered P-waves with high apparent velocity to emerge for a telecom submarine deployment in a very
539 active subduction context, permitting improved analyses in sedimentary basins context. Furthermore, it
540 allows to use traditional magnitude estimation methods based on DAS data to estimate the magnitude of
541 small local events using existing attenuation relationships calibrated with a local seismic network; we
542 demonstrated this in an on-land active normal fault context. Because of the low computational cost of the
543 methods, deformation recovered displacement could be used for earthquake early warning. With the
544 proposed data conversion schemes, we bring DAS data closer to traditional seismological data, permitting
545 the re-use of conventional seismological tools.

546 ACKNOWLEDGMENTS

547 The Stromboli experiment, A.T., F.B, A.S., J.P.M, J.P.M and E.S. were supported by the Agence Nationale
548 de la Recherche (ANR) under the MONIDAS project (Natural Hazard Monitoring using Distributed
549 Acoustic Sensing – ANR-19-CE04-0011). M.E. and D.R were supported by the European Research
550 Council (ERC) under the European Union’s Horizon 2020 research and innovation programme (ABYSS
551 project – grant agreement No. 101041092 – ABYSS). Data and codes used to produce the figures of this
552 manuscript are available at https://github.com/atrabattoni/deformation_seismology_with_das.

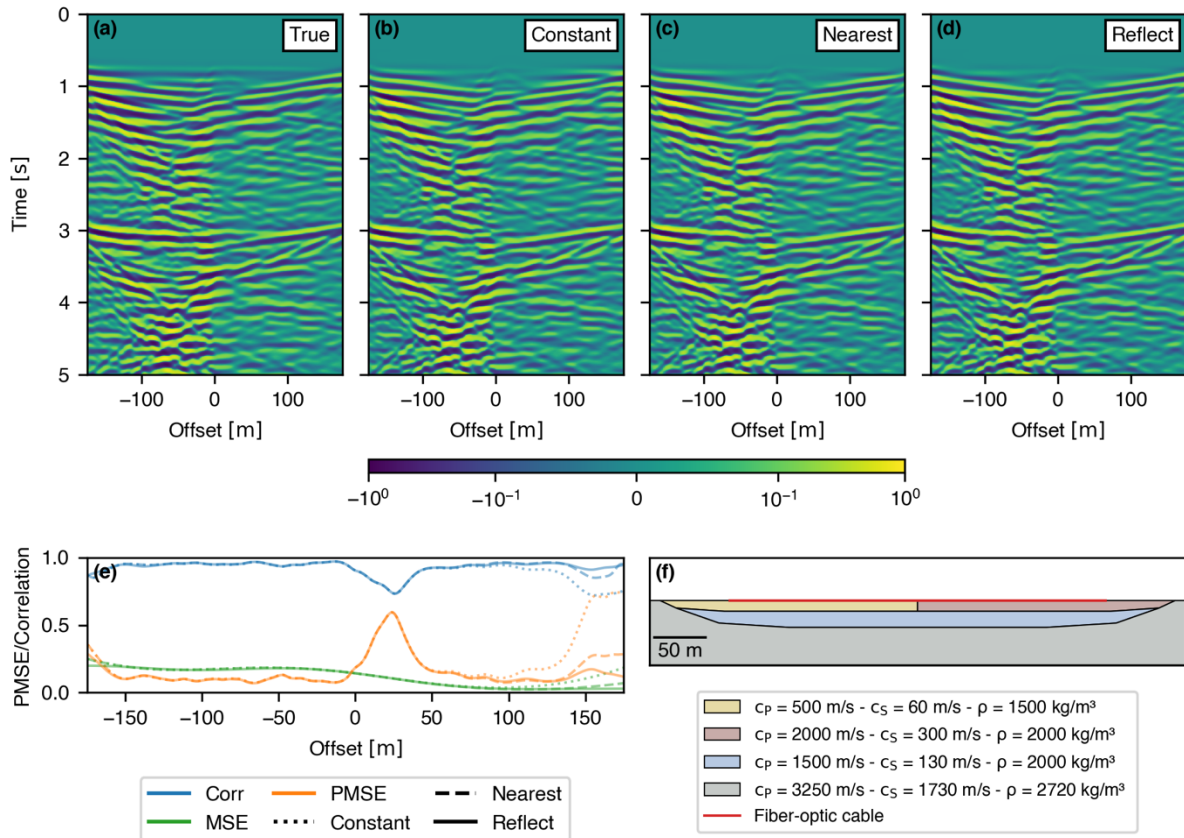
553 REFERENCES

- 554 Biagioli, F., Metaxian, J.-P., Stutzmann, E., Ripepe, M., Bernard, P., Trabattoni, A., Longo, R., & Bouin,
555 M.-P. (submitted). Beamforming Analysis of Seismo-Volcanic Activity with Distributed Acoustic
556 Sensing. *Geophysical Journal International*.
- 557 Bobbio, A., Vassallo, M., & Festa, G. (2009). A Local Magnitude Scale for Southern Italy. *Bulletin of the*
558 *Seismological Society of America*, 99(4), 2461–2470. <https://doi.org/10.1785/0120080364>
- 559 Daley, T. M., Miller, D. E., Dodds, K., Cook, P., & Freifeld, B. M. (2016). Field testing of modular borehole
560 monitoring with simultaneous distributed acoustic sensing and geophone vertical seismic profiles
561 at Citronelle, Alabama: Field testing of MBM. *Geophysical Prospecting*, 64(5), 1318–1334.
562 <https://doi.org/10.1111/1365-2478.12324>
- 563 Fichtner, A., Bogris, A., Nikas, T., Bowden, D., Lentas, K., Melis, N. S., Simos, C., Simos, I., & Smolinski,
564 K. (2022). Theory of phase transmission fibre-optic deformation sensing. *Geophysical Journal*
565 *International*, 231(2), 1031–1039. <https://doi.org/10.1093/gji/ggac237>
- 566 Fossen, H. (2016). *Structural Geology* (2nd ed.). Cambridge University Press.
567 <https://doi.org/10.1017/9781107415096>
- 568 Hartog, A. H. (2017). *An Introduction to Distributed Optical Fibre Sensors* (1st ed.). CRC Press.
569 <https://doi.org/10.1201/9781315119014>
- 570 Lindsey, N. J., Rademacher, H., & Ajo-Franklin, J. B. (2020). On the Broadband Instrument Response of
571 Fiber-Optic DAS Arrays. *Journal of Geophysical Research: Solid Earth*, 125(2).
572 <https://doi.org/10.1029/2019JB018145>
- 573 Lior, I., Rivet, D., Ampuero, J.-P., Sladen, A., Barrientos, S., Sánchez-Olavarría, R., Villarroel Opazo, G.
574 A., & Bustamante Prado, J. A. (2023). Magnitude estimation and ground motion prediction to
575 harness fiber optic distributed acoustic sensing for earthquake early warning. *Scientific Reports*, 13(1),
576 424. <https://doi.org/10.1038/s41598-023-27444-3>
- 577 Lior, I., Sladen, A., Mercerat, D., Ampuero, J.-P., Rivet, D., & Sambolian, S. (2021). Strain to ground motion
578 conversion of distributed acoustic sensing data for earthquake magnitude and stress drop
579 determination. *Solid Earth*, 12(6), 1421–1442. <https://doi.org/10.5194/se-12-1421-2021>
- 580 Marra, G., Clivati, C., Luckett, R., Tampellini, A., Kronjäger, J., Wright, L., Mura, A., Levi, F., Robinson,
581 S., Xuereb, A., Baptie, B., & Calónico, D. (2018). Ultrastable laser interferometry for earthquake
582 detection with terrestrial and submarine cables. *Science*, 361(6401), 486–490.
583 <https://doi.org/10.1126/science.aat4458>

- 584 Martin, E. R., Lindsey, N. J., Ajo-Franklin, J. B., & Biondi, B. L. (2021). Introduction to Interferometry of
585 Fiber-Optic Strain Measurements. In Y. Li, M. Karrenbach, & J. B. Ajo-Franklin (Eds.), *Geophysical*
586 *Monograph Series* (1st ed., pp. 111–129). Wiley. <https://doi.org/10.1002/9781119521808.ch9>
- 587 Mata Flores, D., Mercerat, E. D., Ampuero, J.-P., Rivet, D., & Sladen, A. (2022). *Identification of two vibration*
588 *regimes of underwater fibre optic cables by Distributed Acoustic Sensing* [Preprint]. Geophysics.
589 <https://doi.org/10.1002/essoar.10512896.1>
- 590 Mata Flores, D., Sladen, A., Ampuero, J.-P., Mercerat, E. D., & Rivet, D. (2022). *Monitoring Deep Sea Currents*
591 *with Seafloor Distributed Acoustic Sensing* [Preprint]. Oceanography.
592 <https://doi.org/10.1002/essoar.10512729.1>
- 593 Trabattoni, A., Festa, G., Longo, R., Bernard, P., Plantier, G., Zollo, A., & Strollo, A. (2022).
594 Microseismicity Monitoring and Site Characterization With Distributed Acoustic Sensing (DAS):
595 The Case of the Irpinia Fault System (Southern Italy). *Journal of Geophysical Research: Solid Earth*,
596 *127*(9). <https://doi.org/10.1029/2022JB024529>
- 597 Tromp, J., Komatitsch, D., & Liu, Q. (2008). Spectral-Element and Adjoint Methods in Seismology.
598 *Commun. Comput. Phys.*
- 599 van den Ende, M. P. A., & Ampuero, J.-P. (2021). Evaluating seismic beamforming capabilities of
600 distributed acoustic sensing arrays. *Solid Earth*, *12*(4), 915–934. [https://doi.org/10.5194/se-12-](https://doi.org/10.5194/se-12-915-2021)
601 [915-2021](https://doi.org/10.5194/se-12-915-2021)
- 602 Wang, H. F., Zeng, X., Miller, D. E., Fratta, D., Feigl, K. L., Thurber, C. H., & Mellors, R. J. (2018). Ground
603 motion response to an ML 4.3 earthquake using co-located distributed acoustic sensing and
604 seismometer arrays. *Geophysical Journal International*, *213*(3), 2020–2036.
605 <https://doi.org/10.1093/gji/ggy102>
- 606 Yang, J., Shragge, J., & Jin, G. (2022). Filtering Strategies for Deformation-Rate Distributed Acoustic
607 Sensing. *Sensors*, *22*(22), 8777. <https://doi.org/10.3390/s22228777>
- 608 Yang, Y., Atterholt, J. W., Shen, Z., Muir, J. B., Williams, E. F., & Zhan, Z. (2022). Sub-Kilometer
609 Correlation Between Near-Surface Structure and Ground Motion Measured With Distributed
610 Acoustic Sensing. *Geophysical Research Letters*, *49*(1). <https://doi.org/10.1029/2021GL096503>
- 611

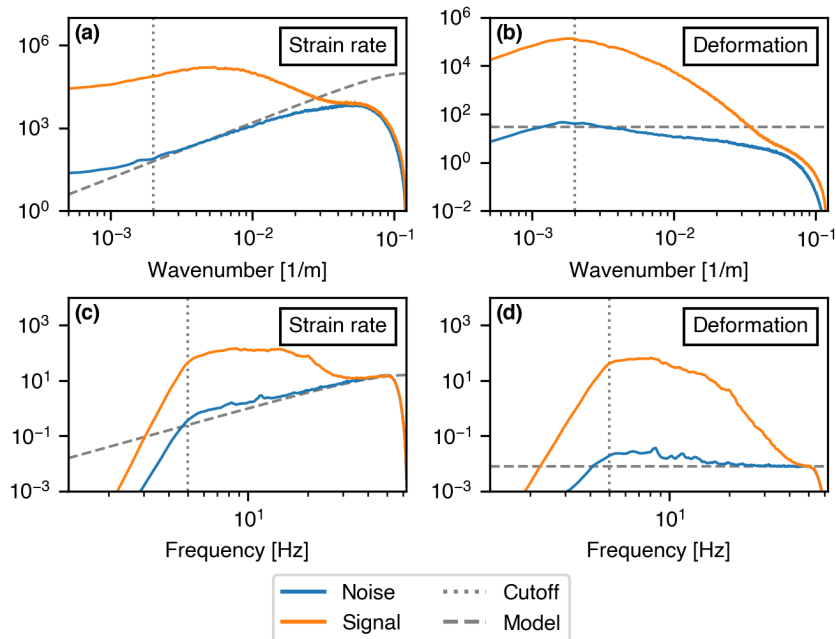
612

SUPPLEMENTARY MATERIAL



613
614
615
616
617

Figure S1. Effects of different padding modes used in the sliding-window scheme. The true velocity (a) is compared with recovered velocity using: (b) constant zero padding, (c) constant closest value padding, and, (d) reflection (or mirror) symmetric padding. Results are mostly identical except at the cable ends. (e) Error metrics for each padding mode. The reflect mode has overall better performances for this case.



618
619
620
621

Figure S2. Noise levels of the OptoDAS interrogator. (a) Average raw strain rate levels in the wavenumber domain for 20 s time windows before (noise in blue) and during (signal in orange) the event presented in Fig 7. (b) Same but for the recovered displacement with a cut-off (vertical dotted grey line) wavelength of

622 500 m associated with the sliding 1 km Hann window used. (c) Raw strain rate levels but in the frequency
623 domain with a clear cut-off frequency of 5 Hz implied by the filtered meant to remove the micro-seismic
624 noise. (d) Same for the deformation-recovered displacement. The strain-rate noise level both increases with
625 the wavenumber and the frequency but less than expected (grey dashed line). If noise was an additive white
626 term in deformation and if strain-rate was computed by simple spatial and temporal differentiation we
627 would expect linearly. It is probable that other derivation schemes are used, that the noise characteristic in
628 deformation is not white and that more advances proprietary processing technics are used.

629



630

631 © 2023. This work is licensed under the Creative Commons Attribution 4.0 International License. To view
632 a copy of this license, visit <http://creativecommons.org/licenses/by/4.0/> or send a letter to Creative
633 Commons, PO Box 1866, Mountain View, CA 94042, USA.